



Analysis of the spray flame structure in a lab-scale burner using Large Eddy Simulation and Discrete Particle Simulation

Damien Paulhiac^{a,b}, Bénédicte Cuenot^{a,*}, Eleonore Riber^a, Lucas Esclapez^a, Stéphane Richard^b

^a CERFACS, CFD Team, 42 Avenue G. Coriolis, Toulouse Cedex 01 31057, France

^b Safran Helicopter Engine, Bordes Cedex 64511, France



ARTICLE INFO

Article history:

Received 30 June 2019

Revised 7 October 2019

Accepted 7 October 2019

Keywords:

Spray

Combustion

Large Eddy Simulation (LES)

Discrete Particle simulation DPS

ABSTRACT

The numerical study of an academic lab-scale spray burner using Large Eddy Simulation coupled with a Discrete Particle Simulation is presented. The objectives are first, to validate current turbulent combustion modeling approach for two-phase flames, and second, to bring new insight on two-phase flame structure in a complex flow, representative of real configurations. The comparison with the experiment shows a good quantitative prediction of the velocity field of the gas and the liquid phases, in both non-reacting and reacting cases. Experimental and numerical results of the spray flame are also in good agreement. The detailed study of the interaction between the flame front and the droplets shows that both single droplet and group combustion regimes occur in the present configuration. These regimes are investigated from the numerical and physical points of view, highlighting the necessity to further investigate their possible importance for the modeling of two-phase combustion.

© 2019 The Combustion Institute. Published by Elsevier Inc. All rights reserved.

1. Introduction

Most industrial gas turbines use a direct injection system to introduce the liquid fuel into the combustion chamber. These injection systems generate a dilute spray of very small droplets, enhancing the dispersion and evaporation processes of liquid fuel. To optimize the performance of today's engines and reach the more and more restricting efficiency and pollution targets, a deep knowledge of the mechanisms controlling the strong interaction between the spray, the turbulence and the combustion is necessary. Two-phase combustion has thus been extensively studied in the literature, and was recently reviewed in [1] for dilute reacting sprays. It has been demonstrated theoretically that various droplet combustion modes may occur, as described by Chiu [2] or Annamalai and Ryan [3]. These modes range from single droplet combustion, where a flame stabilizes in the close vicinity of one isolated droplet, to group combustion, where the flame stands outside a cloud of droplets. Evaporation and fuel consumption rates may differ dramatically in these two extreme regimes, and lead to different burner performances, in terms of flame

Nomenclature

PLIF	Planar Laser Induced Fluorescence
LDA	Laser-Doppler Anemometry
I_{flame}	Takeno flame index [59]
HR	Heat release
PDF	Probability Density Function

length, flame stabilization, maximum temperature or pollutant emissions.

Experiments range from the simplest configurations of single droplet and droplet array combustion, to complex spray burners. Single droplet combustion experiments are numerous (for example [4–6]) and highlight the possible existence of a spherical diffusion flame standing around the droplet at a distance of about ten droplet radii. Streams or arrays of droplets are used to understand the mechanism of interaction between droplets and flame propagation inside a cloud of droplets [3]. Depending on the inter-droplet spacing and droplet size, the flame is able to propagate or not in the droplet mist, with different mechanisms of propagation (premixed flame propagation, non-premixed flame growth and transmission, ignition of neighboring drops by heat diffusion [7]). Moreover, the flame propagation speed is found maximum when

* Corresponding author.

E-mail addresses: cuenot@cerfacs.fr, benedicte.cuenot@cerfacs.fr (B. Cuenot).

the inter-droplet spacing is of the order of the droplet flame radius. When droplets mainly evaporate before reaching the flame front, the premixed-like laminar flame speed is shown to be, on the one hand, reduced compared to the equivalent purely gaseous flame speed because of evaporation effects [8], and on the other hand, increased in some cases due to chemical effects [9] or thermal expansion of the burnt gases [7]. Going to more complex sprays, Marley et al. [10,11] studied a lifted flame stabilizing near a conical spray, and featuring a well known “triple flame” structure. Preferential segregation of droplets [12] is observed and is shown to play a role in the stabilization of the flame: smaller droplets, which evaporate faster, mix better with the oxidizer, generating a mixture sufficiently rich to stabilize the triple flame leading edge; larger droplets, which tend to have a ballistic behavior, are convected downstream and feed an outer diffusion flame. Richard et al. [13] studied a Lean Pre-vaporized Premixed (LPP) burner, consisting of an air-assisted atomizer placed at the center of a cylindrical tube surrounded by a coflow of turbulent air, in which the amount of pre-vaporation was varied along with other parameters. The two-phase flame was stabilized thanks to a pilot flame. The degree of prevaporation was found to increase when the inlet temperature or the fuel volatility increased, and the global equivalence ratio or the mean droplet diameter at injection decreased. Gounder et al. [14] and Kourmatzis et al. [15] studied more recently a well instrumented spray burner, fed with well controlled droplets generated by an ultrasonic atomizer, embedded in a coflow of turbulent air. The flame was also stabilized by a pilot flame. Likewise, the influence of the fuel volatility, the coflow injection speed, the droplet size and the turbulent dispersion were analysed and found to be important. All these configurations are particularly well suited for numerical code validation. However, they represent only partially industrial applications, where the flame stabilization is generally obtained by a recirculating swirling flow and does not require a pilot flame device.

In more realistic configurations, Widmann and Presser [16,17] measured the properties of a hollow cone spray within a confined swirled turbulent jet of air. Lecourt and coworkers [18] studied a confined swirled spray burner very similar to an aeronautical injection system, with preheated air. Marchione et al. [19] designed a confined burner to analyze the stochastic ignition process in a spray configuration. The flow was swirled and the n-heptane flame was stabilized behind the bluff body holding the injector. A similar configuration was recently operated by Cavaliere et al. [20] to analyze two-phase flame structures. Various spray flame regimes were found and investigated with combined measurements of the flame, gas and liquid phases, allowing a detailed analysis of the spray flame and providing a comprehensive set of data for the validation of numerical simulations.

On the numerical side, Direct Numerical Simulation (DNS) resolving all scales, from the droplet internal flow to the largest turbulent eddies, are becoming standard, but are still limited to very small domain and number of droplets. In addition they often use simplified approaches (simplified geometry, chemistry, etc). DNS of spherical droplets have shown typical single droplet behaviors such as wake and envelope flames [21], droplet-droplet interactions [22], or hysteresis behavior [23]. It was demonstrated that the burning mode has a strong influence on the level of NO_x emissions [24]. If the spray is dilute and the droplet is smaller than the smallest turbulent scales, Discrete Particule Simulation (DPS) may be used where droplets are treated as point sources, without resolving the flow in the droplet [25]. DPS was coupled to DNS of turbulent flow to study spray/turbulence interaction [12,26], highlighting preferential segregation mechanisms. This DNS-DPS approach was later extended to reacting cases [27–32], featuring various two-phase combustion regimes. Depending on the evaporation time scale and inter-droplet spacing, combustion regimes can

Table 1

Operating conditions of the Cambridge burner, case SWH1 [40].

Air bulk velocity	14.8 m/s
Air temperature	300 K
Chamber pressure	1 atm
Fuel flow rate	0.12 g/s
Fuel temperature	300 K
Mean diameter at injection	40 μm
Spray mean angle	38°
Global equivalence ratio	0.17

be divided into three different groups: external combustion, where the flame stands outside the spray, group combustion, where small pockets of droplets burn, and hybrid combustion, combining the two previous regimes. In particular, a 3D DNS-DPS of a complex swirled configuration with simplified chemistry was undergone by Luo et al. [33] and showed the extreme complexity of the spray flame structure, yielding strong heterogeneities of equivalence ratio and intricating premixed and non-premixed flames.

In realistic geometries, for which DNS-DPS is still too computationally costly, less CPU demanding approaches such as Reynolds Averaged Navier-Stokes (RANS) or Large Eddy Simulations (LES) are coupled with DPS to compute turbulent two-phase flows. RANS-DPS gives good results [34], but reduces the droplet-turbulence interaction to the mean flow. In the LES approach, the explicit resolution of the large turbulent scales allows to take into account the subtle interactions between turbulence, spray and combustion. Many complex two-phase spray flames have recently been computed using LES-DPS [35–39] showing encouraging results when compared to available experimental data. However, a detailed analysis of the spray flame structures in such complex flows has not been proposed yet. In this paper, LES-DPS is used to study the experiment of Cavaliere et al. [20], where a complex two-phase flame structure has been observed. After verifying the accuracy of the modeling approach by quantitative comparisons with measurements, the two-phase flame structure is analyzed in detail to gain new insight in the two-phase combustion processes in complex flows.

2. Experimental setup

The experimental burner of Cavaliere et al. was designed at the University of Cambridge in order to obtain a swirl-stabilized flame on which to apply a variety of diagnostics [20]. The geometry consists of a 350mm-long vertical circular duct in which a conical bluff-body is embedded, leading to a rectangular chamber made of synthetic optical-quality quartz and open to the atmosphere (Fig. 1). A swirler placed in the duct gives a 60-degrees precessing motion to the cold incoming air flow. The pressure swirl hollow-cone atomizer (manufactured by Lechler), with a nozzle exit diameter of 0.15 mm and imbedded in the bluff-body, creates a 80-degrees hollow-cone spray in the chamber [20]. The liquid fuel is n-heptane, chosen for its fast evaporation, which allows the spray flame to stabilize without air preheating. The simulated operating point labeled SWH1 in [40] corresponds to the conditions given in Table 1. Cold air and fuel are injected in the chamber at atmospheric pressure with a lean global equivalence ratio of 0.17.

Thanks to the transparent walls of the chamber, axial and tangential velocities of the gaseous phase could be measured using Laser-Doppler Anemometry (LDA) at various sections in the combustion chamber for both non-reacting and reacting cases. Since LDA results are perturbed by the presence of liquid droplets, gaseous velocity measurements are valid only outside the spray region. The spray was qualitatively measured via Mie-scattering. The flame-front location was evaluated with OH-Planar Laser Induced Fluorescence (OH-PLIF). Droplet velocities were also

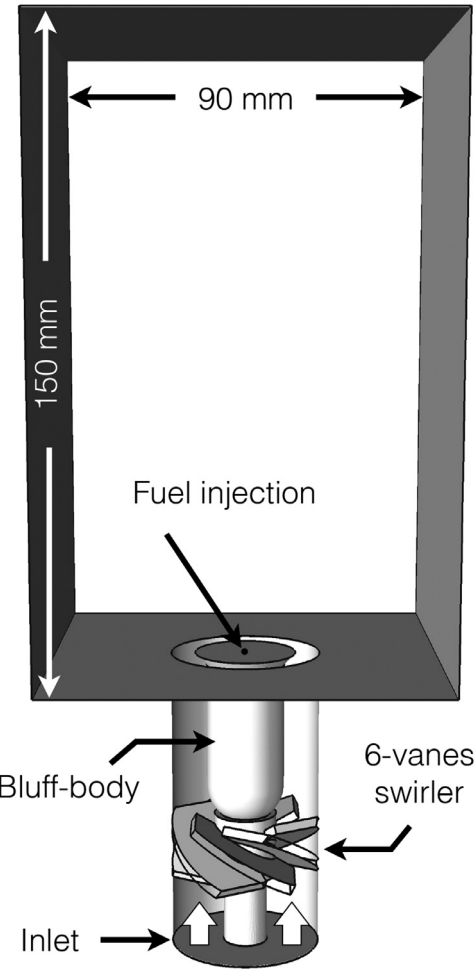


Fig. 1. Computational domain for the Cambridge burner [20].

measured [41] at various axial locations using Phase Doppler Anemometry (PDA). Species emission data were obtained at several points along the middle plane at the chamber exit.

3. Governing equations and numerical set-up

Gaseous phase

The LES filtered compressible Navier–Stokes equations read for the multi-component, compressible gas flow:

$$\frac{\partial \bar{\rho} \tilde{u}_i}{\partial t} + \frac{\partial}{\partial x_j} (\bar{\rho} \tilde{u}_i \tilde{u}_j) = - \frac{\partial}{\partial x_j} [\bar{P} \delta_{ij} - \bar{\tau}_{ij} - \bar{\tau}_{ij}^t] + S_{u,i}^{l \rightarrow g}, \quad (1)$$

$$\begin{aligned} \frac{\partial \bar{\rho} \tilde{E}}{\partial t} + \frac{\partial}{\partial x_j} (\bar{\rho} \tilde{E} \tilde{u}_j) = & - \frac{\partial}{\partial x_j} [\bar{u}_i (\bar{P} \delta_{ij} - \bar{\tau}_{ij} - \bar{\tau}_{ij}^t) + \bar{q}_j + \bar{q}_j^t] \\ & + \bar{\omega}_T + \bar{Q}_r + S_{E,i}^{l \rightarrow g}, \end{aligned} \quad (2)$$

$$\frac{\partial \bar{\rho} \tilde{Y}_k}{\partial t} + \frac{\partial}{\partial x_j} (\bar{\rho} \tilde{Y}_k \tilde{u}_j) = - \frac{\partial}{\partial x_j} [\bar{J}_{j,k} + \bar{J}_{j,k}^t] + \bar{\omega}_k + S_k^{l \rightarrow g}, \quad (3)$$

where ρ is the gaseous mass density, u the velocity, E the total energy, and Y_k the mass fraction of specie k . Einstein's rule of summation is used, $\bar{\cdot}$ corresponds to spatial average, and $\tilde{\cdot}$ to Favre average. The filtered stress tensor $\bar{\tau}_{ij}$ in Eq. (1) and diffusive fluxes \bar{q}_j (Eq. (2)) and $\bar{J}_{j,k}$ (Eq. (3)) are directly computed with filtered variables assuming negligible higher-order correlations. The classical Sutherland law [42] is used for the mixture viscosity, combined

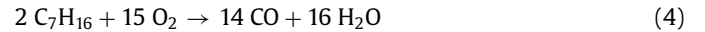
Table 2

Characteristics of inlet conditions for laminar diffusion counterflow flames. Temperature and species mass fractions.

	Fuel side	Air side
T	1200 K	300 K
Y_{Fuel}	27%	0%
Y_{O_2}	0%	23%
Y_{N_2}	52%	77 %
Y_{CO_2} & $Y_{\text{H}_2\text{O}}$	21%	0%

with constant species Schmidt numbers Sc_k and Prandtl number Pr to calculate species diffusion and heat conductivity, respectively. A correction diffusion velocity is added to species diffusion to ensure mass conservation. The turbulent stress tensor $\bar{\tau}_{ij}^t$ is modeled using the WALE subgrid-scale model [43], while the turbulent heat conduction term \bar{q}_j^t and species diffusion $\bar{J}_{j,k}^t$ are modeled by introducing turbulent Prandtl and Schmidt numbers ($Pr_t = Sc_t = 0.6$), respectively. The terms $S_*^{l \rightarrow g}$ correspond to the mass, momentum and energy transfers from the liquid dispersed phase to the gaseous phase, and are detailed later in this Section. Eqs. 1 to 3 are numerically solved with the code AVBP developed by CERFACS/IFPEN [44], using an explicit 3rd order numerical scheme in space and time [45].

Combustion chemistry is described with a global two-step scheme for n-heptane/air flame chemistry, named 2S_C7H16_DP, that was fitted against measured laminar flame speeds following the methodology proposed by Franzelli et al. [46]. It includes the reaction of n-heptane into CO as well as the equilibrium reaction between CO and CO₂ to correctly reproduce the burnt gas temperature and composition for rich mixtures:



In addition, in order to recover the correct flame speed of rich flames, the pre-exponential factors of the two reactions are corrected depending on the local equivalence ratio [47]. The chemical parameters and correction functions are described in Appendix A.

The scheme 2S_C7H16_DP was first evaluated in freely-propagating 1D premixed flames using CANTERA [48] by comparison with a 65-species/315 reactions detailed mechanism [49]. Figure 2(left) shows that the reduced scheme accurately reproduces the adiabatic flame temperature and the flame speed, for equivalence ratios ranging from 0.7 to 1.4 at atmospheric pressure and ambient temperature, which corresponds to the conditions of the target experiment.

As this burner mainly generates a non-premixed flame (see Section 5), the 2S_C7H16_DP scheme was also evaluated in laminar diffusion counterflow flames at different strain rates. For these test cases, inlet conditions were again chosen representative of the target experiment and are summarized in Table 2. Figure 2(right) displays the comparison with detailed chemistry in terms of total heat-release rate, i.e., integrated across the flame front, for strain rates in the range [10 s⁻¹–100 s⁻¹] as found in the experiment. It is found that the reduced scheme correctly reproduces the detailed chemistry behavior: the total heat release rate increases with the strain rate, with however a slightly larger slope. As the maximum difference is of the order of 20% at the highest strain rate, the accuracy of the reduced scheme is considered sufficient for the purpose of the present study.

The premixed flame thickness of heptane-air flames in ambient conditions varies between 1 and 2.5 mm. Considering the relatively small size of the configuration, it is possible to use a sufficiently refined grid ($\Delta x \sim 0.2$ mm in the flame region) to

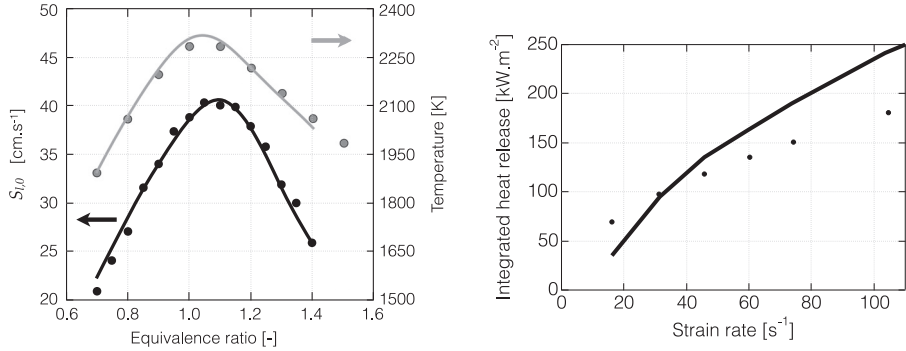


Fig. 2. Comparison between detailed chemistry [49] (symbols) and reduced chemistry 2S_C7H16_DP (lines). Left: flame speed (black) and equilibrium temperature (gray) in a 1D freely propagating flame. Right: Total heat release versus strain rate in a counterflow diffusion flame.

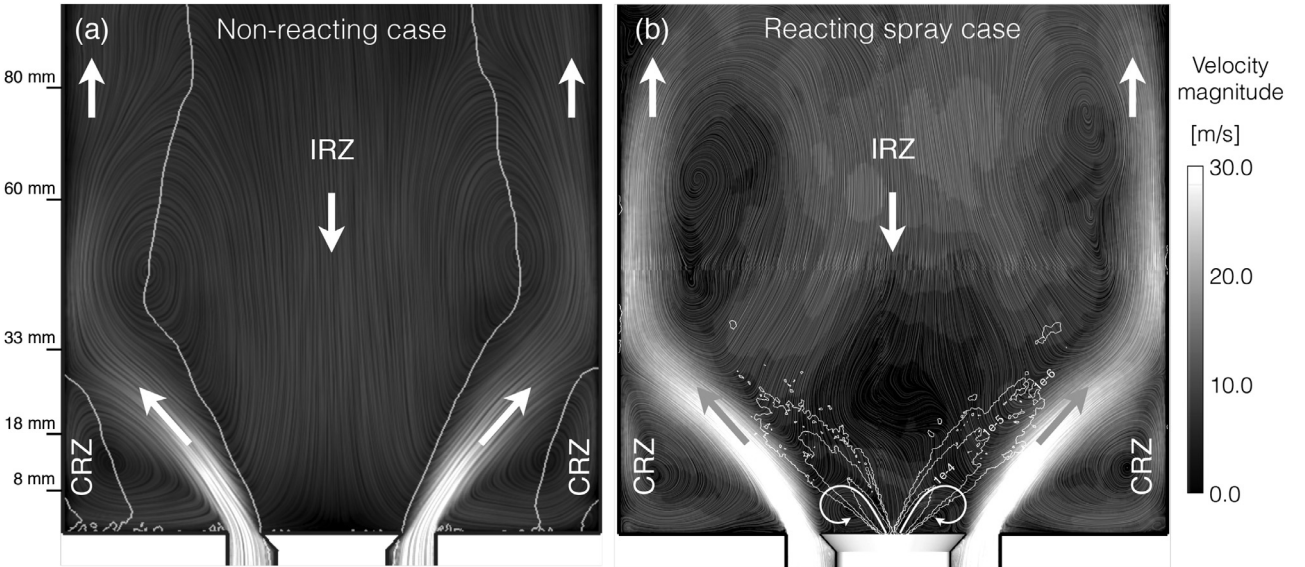


Fig. 3. Time-averaged field of velocity magnitude in the middle plane of the chamber. (a) non reacting gaseous case (isoline of zero axial velocity). Right : reacting spray case (isoline of liquid volume fraction). The white lines indicate small recirculating structures due to the spray injection.

resolve the flame front, which allows to compute directly the filtered chemical source terms $\bar{\omega}_k$ and \bar{Q}_r from filtered variables using Arrhenius laws. The flame front resolution will be checked *a posteriori* by analysing the LES solutions (Sections 4.2 and 5).

Liquid phase

Under the assumptions of dilute spray and small spherical particles, the Lagrangian equations for droplet motion and energy in the DPS approach are written as:

$$\frac{dX_p}{dt} = u_p \quad (6)$$

$$\frac{dm_p u_p}{dt} = F_p \quad (7)$$

$$\frac{dm_p}{dt} = \dot{m}_p \quad (8)$$

$$\frac{dC_{p,l} T_p}{dt} = \frac{1}{m_p} (-\Phi_g^c + \dot{m}_p L_v(T_p)) \quad (9)$$

with X_p the droplet position, u_p its velocity, m_p its mass, T_p its temperature, and $C_{p,l}$ the liquid heat capacity which varies with temperature. Liquid density is assumed constant. F_p are the sum of all external forces acting on the droplet, \dot{m}_p is the evaporation rate, L_v the latent heat of evaporation and Φ_g^c the gaseous conductive heat flux at the surface of the droplet. In the conditions of the

target configuration, $F_{i,p}$ in Eq. (7) reduces to the stationary drag force expressed as :

$$F_p = \mathbf{F}_D = \frac{1}{2} \rho C_D A \|u - u_p\| (u - u_p) \quad (10)$$

where $A = \pi d_p^2 / 4$, with d_p the droplet diameter, is proportional to the droplet surface area, and C_D is a function of the particle Reynolds number Re_p , following Schiller and Nauman [50] for $Re_p \leq 800$:

$$C_D = \frac{24}{Re_p} \left[1 + 0.15 Re_p^{0.687} \right] \quad (11)$$

with

$$Re_p = \frac{\rho \|u - u_p\| d_p}{\mu} \quad (12)$$

where μ is the gas viscosity.

The source terms \dot{m}_p and Φ_g^c are obtained following the evaporation model of Abramzon and Sirignano [51], with thermodynamic and transport properties in the vicinity of the droplet computed from the local mixture composition, as detailed in [52,53], and leading to Prandtl and Schmidt numbers at the droplet surface of 0.85 and 0.95, respectively. All gaseous quantities needed to evaluate the various source terms of the droplet equations are evaluated by linear interpolation at the position of the particle, assuming that the flow field is locally undisturbed by the presence

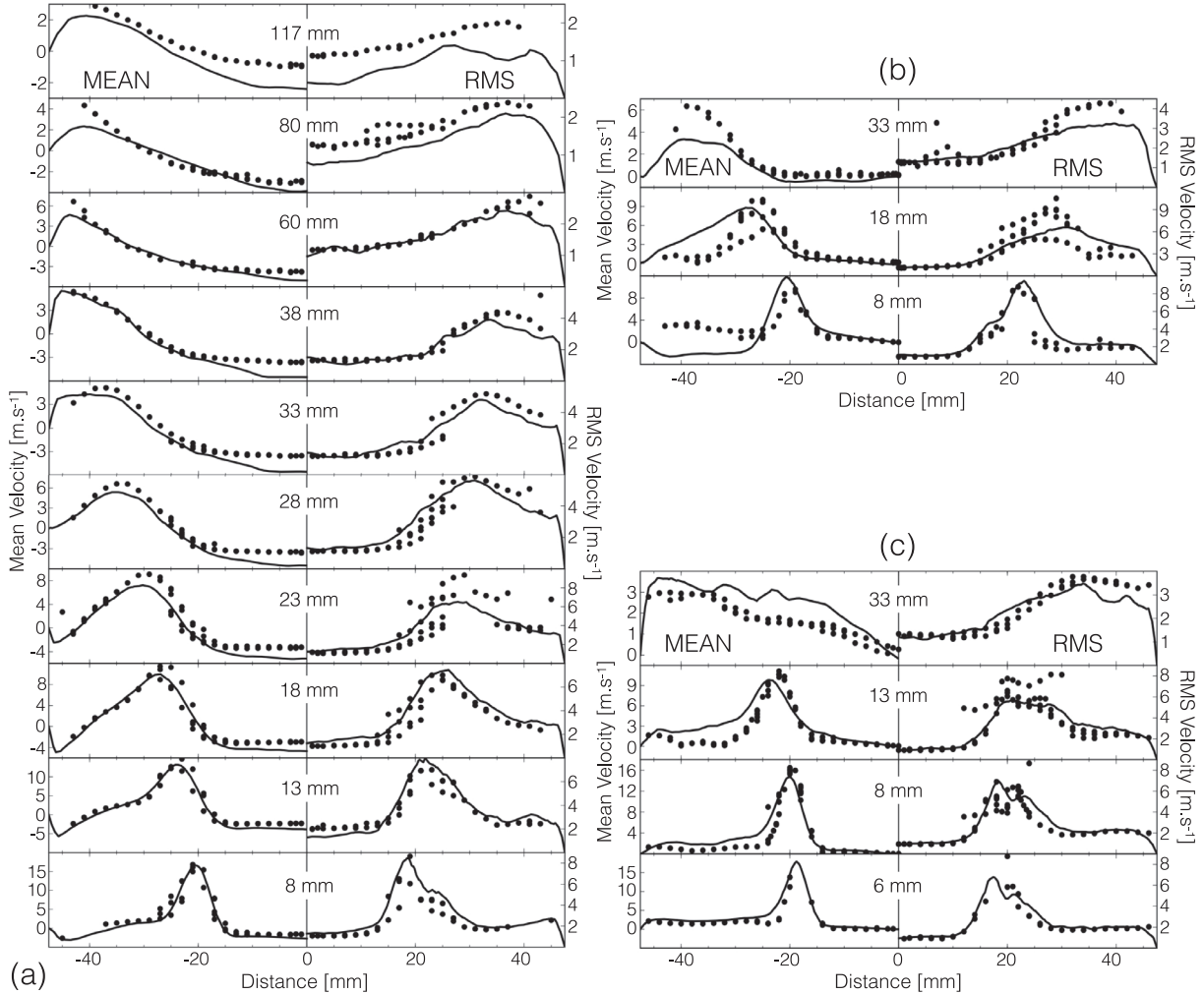


Fig. 4. Non reacting gaseous case: LES (lines) versus experiment (symbols) [40]. Profiles of mean (left half) and RMS (right half) gas velocity at axial locations downstream the injection (see Fig. 3(a)): (a) axial component, (b) radial component, (c) azimuthal component.

of this particle [54,55]. Note also that, thanks to the high grid refinement in the spray zone, the subgrid-scale effects on droplet dynamics can be neglected.

Using the FIM-UR model [56] applied to the injector characteristics of the experiment, a fully atomized, conical spray is built and injected at the atomizer exit. The droplet size distribution follows a Rosin-Rammler shape with a Sauter Mean Diameter (SMD) $d_p^{SMD} = 40\mu m$, a spread factor $q = 2.5$ (Eq. (13)), and the cone half-angle is 38° . The droplet injection velocity is built from correlations following [56]. Due to the lack of more detailed measurements, some uncertainty is associated to the injected spray characteristics, which should be kept in mind when analysing the LES results.

$$RR(d_p) = q \frac{d_p^{q-1}}{X^q} \exp\left(-\frac{d_p^q}{X}\right) \quad (13)$$

with

$$X = \frac{\Gamma(1 + 2/q)}{\Gamma(1 + 2/q)} d_p^{SMD} \quad (14)$$

where Γ is the usual Gamma function and d_p^{SMD} is the Sauter Mean Diameter.

The two-way coupling between liquid and gaseous phases is ensured by a first order interpolation between droplet positions

and grid nodes, giving source terms to the gaseous equations as:

$$S_u^{l \rightarrow g} = \frac{1}{\Delta V} \sum_{n=1}^N \Psi(x_p^n) \left(-m_p^n F_D^n + \dot{m}_p^n u_p^n \right) \quad (15)$$

$$S_E^{l \rightarrow g} = \frac{1}{\Delta V} \sum_{n=1}^N \Psi(x_p^n) \left(-m_p^n F_D^n \cdot u_p^n + \frac{1}{2} \dot{m}_p^n \|u_p^n\|^2 - \dot{\Phi}_p^n \right) \quad (16)$$

$$S_{Fuel}^{l \rightarrow g} = \frac{1}{\Delta V} \sum_{n=1}^N \Psi(x_p^n) \dot{m}_p^n \quad (17)$$

where ΔV is the mesh element volume, N the number of droplets in this volume and $\Psi(x_p)$ a first-order interpolation function between the particle position and the grid nodes of the cell.

The computational domain (Fig. 1) includes all geometrical details of the experiment configuration, i.e., the swirler, the bluff-body and the co-flow cylinder. The mesh spatial discretization is fine enough in the duct and through the swirler, to correctly develop and transport turbulence in the chamber. A large spherical atmospheric plenum (not shown) is added to the chamber exit to minimize the influence of outlet boundary conditions. As already mentioned, the primary zone of the chamber where the flame stabilizes is sufficiently refined to resolve the turbulent flame front.

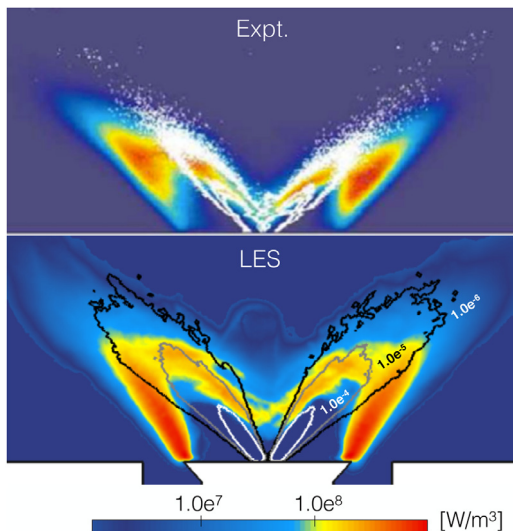


Fig. 5. Two-phase reacting case: experiment (top) vs LES-DPS (bottom). Top: time-averaged OH-PLIF imaging (grey levels) and MIE scattering (white) [20]. Bottom: LES-DPS time-averaged field of heat-release and liquid volume fraction iso-contours.

Characteristic boundary conditions are applied to the inlet and outlet [57]. Adiabatic non-slip walls are used everywhere, except at the top of the bluff-body where heat-losses are imposed. Consistently with experimental observations, the heat flux is evaluated at this surface with a reference temperature of 400K and a heat transfer coefficient of $6.7 \text{ m}^2/\text{K/W}$. These parameters mostly impact the stabilization of the flame, which is correctly predicted with the chosen values. However there is some uncertainty on the resulting heat loss, which should be kept in mind in the analysis of Section 5.1.

4. Validation of LES-DPS: comparison with experiment

4.1. Non-reacting case

The ability of LES to reproduce the main features of the experiment is checked for the SWH1 operating conditions of Table 1, in the case of non-reacting gaseous flow. Due to the swirling motion, a large and long Inner Recirculation Zone (IRZ) appears in the center of the chamber, accompanied by two smaller Corner Recirculation Zones (CRZ) (Fig. 3(a)). The swirled jet of fresh air impinges the sidewalls of the chamber, then flows along the walls downstream to the outlet.

Figure 4 shows that the simulation correctly reproduces the jet opening and the location and size of the recirculation zones, as demonstrated by the quantitative comparison of the mean velocity radial profiles at several axial locations through the chamber (see Fig. 3(a)). Moreover, LES also captures the correct levels and profile shapes of velocity fluctuations in the three directions.

4.2. Reacting case

In the SWH1 reacting case, a quasi-axisymmetric M-shaped flame stabilizes behind the bluff-body, engulfing the liquid spray. A qualitative comparison with experimental images (Fig. 5) shows a good overall agreement, in terms of spray angle, droplet dispersion, and flame localization. In both LES and experiment, droplets crossing the main reaction zone are observed. This is of particular interest, as it leads to different droplet combustion regimes. In the experiment the center of the flame is shown in average to be closer to the bluff body than in the LES (3 mm above the bluff

body surface in the experiment vs 7 mm in the LES). At that particular location, no droplets are found in the simulation contrary to what is observed in the experiment, which can be due to the above-mentioned uncertainties on the injected spray. In particular, the hollow-cone spray injected in the simulation does not contain droplets along the centerline, preventing the flame to stabilize further upstream.

In order to check *a posteriori* that the grid resolution is sufficient, the effective flame front resolution has been evaluated in the LES solutions and found to be of the order of 3 to 6 cells in the flame thickness, which is indeed enough to resolve the flame structure. Moreover the fine grid leads to negligible subgrid-scale flame-turbulence interactions, so that no turbulent combustion model is required.

The time-averaged integrated heat-release rate in the LES is 4.9 kJ/s, corresponding to a burning efficiency of 90%. To compare with, the experimental burner efficiency estimated from the unburnt hydrocarbons measured along a radial line near the exit of the chamber [41], was found to be about 88%, which is close to the LES results.

Figure 6 (a) shows that the time-averaged temperature is maximum at the average flame position, and diffuses inside and outside the M-flame. Inside the M-flame, the high gas temperature enhances spray evaporation, leading to a very high mass fraction of fuel. Both heat losses and evaporation heat transfer locally decrease the temperature in the vicinity of the bluff-body. As no air is injected with the spray, and the outer M-flame is mostly attached to the bluff-body, it is mainly a purely non-premixed flame, burning fuel vapor of the inner side with fresh air of the outer side, both mixed with hot products. Note that the evaporation zone crosses and extends outside the M-flame, leading to complex flame structures as will be shown in Section 5.

To further analyze the flame, and compare with the non-reacting gaseous case, the two-phase reacting mean gaseous flow structure is shown in Fig. 3(b). Similarly to the non-reacting gaseous case, the swirled air injection generates small CRZ and an IRZ. Figure 6(b) shows the impact of the IRZ on mixing with the instantaneous mixture fraction Z , defined as in Bilger [58] (leading to the stoichiometric mixture fraction $Z_{st} = 0.062$). Inside the M-flame, the mixture fraction varies between 0 and 0.35, corresponding to the mixing of fuel vapor with hot products issued from the diffusion flame. Outside the M-flame, the mixture fraction corresponds either to the air flow (on the sides) with a minimum value of 0, or to a mixture of air and hot products near the overall equivalence ratio (on the top) with a minimum value of 0.011. Depicted in Fig. 3(b) with white lines, the presence of the spray in the two-phase reacting case generates a small additional recirculating flow feature in the spray region near the bluff body. In this region, the momentum exchange of the gas and the hollow-cone spray generates intense vortical structures that are enclosed in the M-flame envelope. These vortical structures have an intermittent behavior, also clearly observed in the experiment, and sketched in Fig. 7. They first grow until reaching a size of about half the M-shape width. Then they locally quench the flame, ejecting hot products, fuel vapor and droplets outside the flame envelope. Finally they are dissipated, allowing the flame to re-attach to the bluff body.

To consolidate the validation, quantitative comparisons are presented in Figs. 8 and 9. The gas mean and RMS axial and tangential velocity profiles displayed in Fig. 8 at three axial locations show that LES-DPS results reproduce correctly the flow with the correct jet opening angle and peak positions and levels. A slight over-prediction of velocity fluctuations close to the bluff body is observed, probably due to the already mentioned small different location of the flame.

Concerning the liquid phase, arithmetic average of liquid quantities, without size or mass weighting, are compared. Liquid

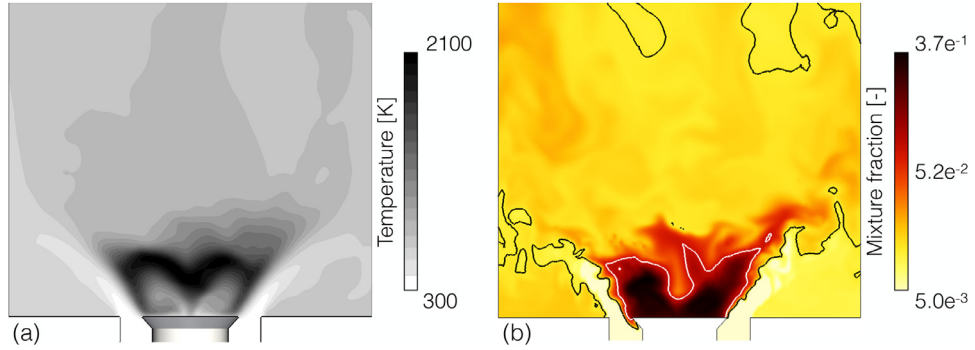


Fig. 6. (a) LES-DPS time-averaged temperature field. (b) Instantaneous mixture fraction field. White iso-contour indicates the stoichiometric mixture fraction and black iso-contour indicates the overall equivalence ratio ($Z_{\phi_g} = 0.0111$).

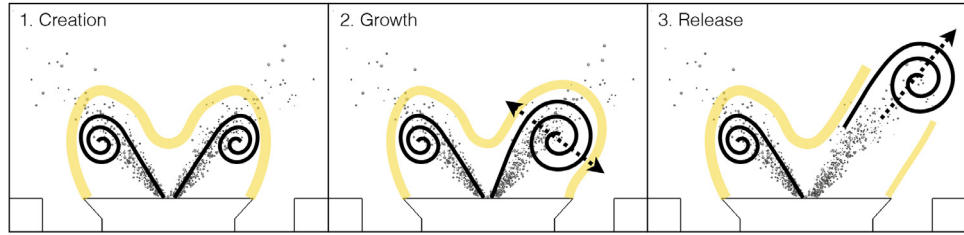


Fig. 7. Intermittent behavior of vortical structures generated by the coupling between the injected spray and the gas phase.

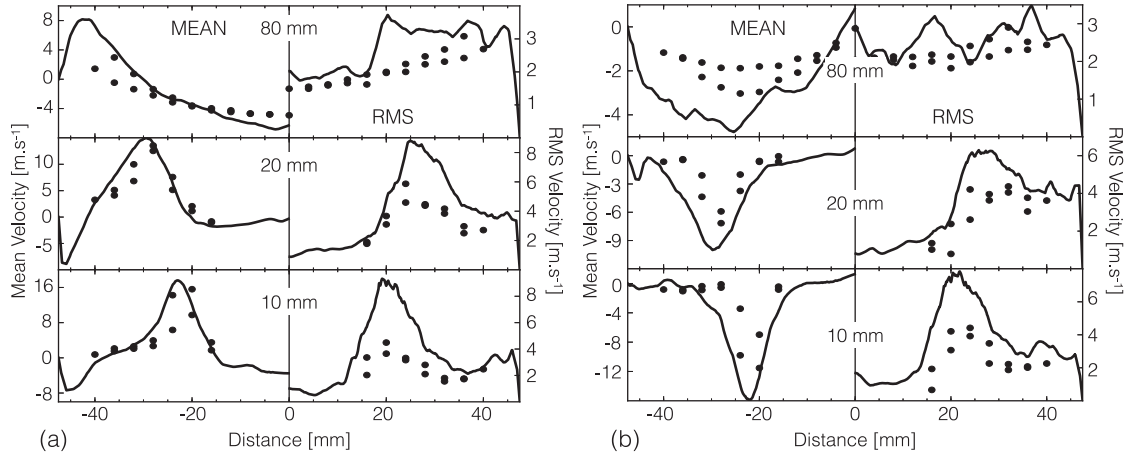


Fig. 8. Two-phase reacting case: LES-DPS (lines) versus experiment (symbols) [40]. Profiles of axial (a) and tangential (b) mean (left) and RMS (right) gaseous velocity at three axial locations downstream the injection (see Fig. 3(a)).

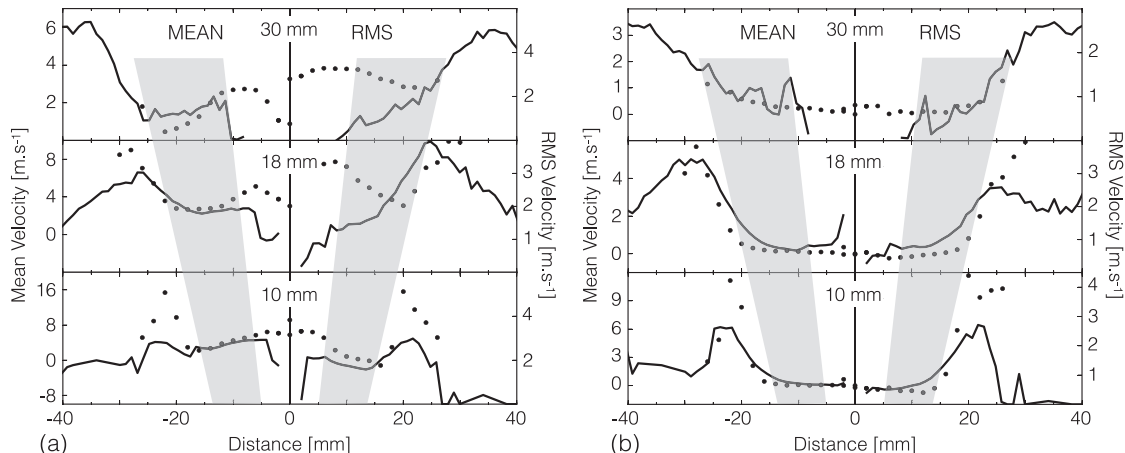


Fig. 9. Two-phase reacting case: LES-DPS (lines) versus experiment (symbols) [41]. Profiles of mean (left) and RMS (right) axial (a) and tangential (b) droplet velocity at 3 locations downstream the injection (see Fig. 3(a)). The core region of the spray is highlighted in grey.

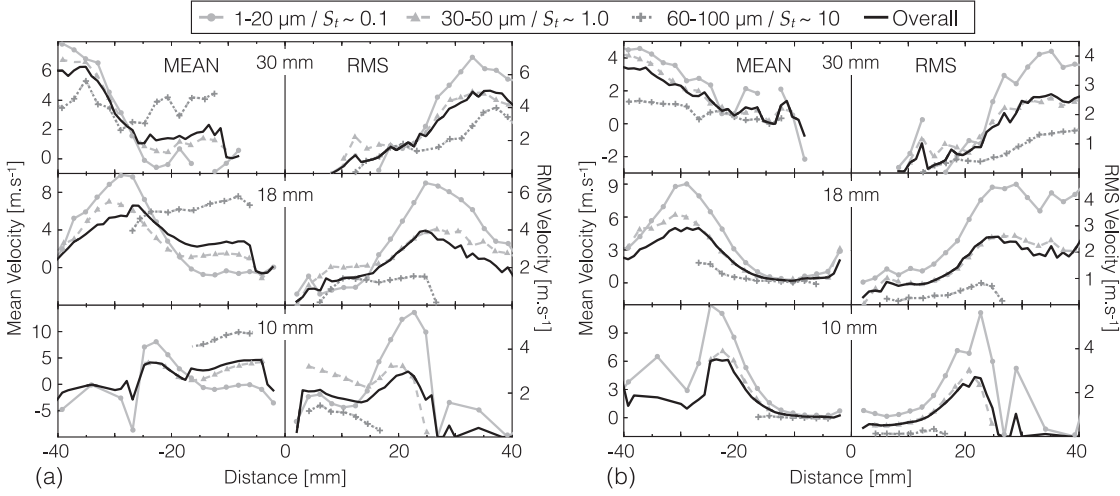


Fig. 10. Two-phase reacting case: profiles of mean (left) and RMS (right) axial (a) and tangential (b) droplet velocity at 3 locations downstream the injection (see Fig. 3(a)). Comparison of 3 different classes of diameters extracted from the LES-DPS, compared to the overall mean liquid velocity.

velocity profiles, shown at three different sections in Fig. 9, indicate a good agreement in the central core of the injection cone (grey zones in Fig. 9). Outside this region, some differences appear, that may originate from two sources. First, as observed in the comparison with Mie-scattering in Fig. 5, the LES-DPS spray contains less droplets in the center. Second, even a small uncertainty on the injected droplet size distribution may lead to a significant error on the mean velocity because large, medium and small droplets have different inertial behaviors. This is illustrated in Fig. 10 where droplet size-conditioned mean liquid velocity profiles are shown. The three droplet size-classes are defined as small ($d_p < 20\mu\text{m}$), medium ($20\mu\text{m} < d_p \sim 60\mu\text{m}$) and large ($d_p > 60\mu\text{m}$), approximately corresponding to Stokes numbers of 0.1, 1 and 10, respectively. It appears clearly that the three classes of droplets contribute very differently to the arithmetic mean liquid velocity: medium size droplets have a velocity close to the overall average, while small size droplets, which are much more sensitive to the gaseous flow, exhibit higher velocity fluctuations, and on the contrary large size droplets keep more constant velocity profiles. As a consequence, arithmetically averaging flow quantities may increase error levels, especially in regions of low mass loading at the spray borders. More detailed measurements including the local size distribution of droplets would be helpful to improve the comparison.

5. Flame structure analysis

In the thin M-shape flame observed in both experiment and simulation, four distinct regions of the flame-front may be distinguished and are identified in Fig. 11. The middle V-shaped part of the flame, labeled I, yields a smooth flame front, stabilized near the bottom of the IRZ along the stoichiometric line. The side conical branch of the flame, labeled II, consists in a highly wrinkled flame front that stabilizes between the air flow and the edge of the bluff-body at a fluctuating distance from the injection plane. In these two regions, the flame is purely gaseous, i.e., without droplet inside the reaction zone, and is fueled by the pre-evaporation of droplets. The two other regions, labeled III and IV, feature a complex flame structure, where the spray directly interacts with the reacting zone, leading to different two-phase combustion regimes. In region III, a flame front very similar to the flame in I and II is observed, except that droplets are not fully evaporated before entering the reaction zone, and continue to evaporate inside it. In region IV, droplets that have survived the flame region III, are surrounded by fresh air and combustion occurs very locally around

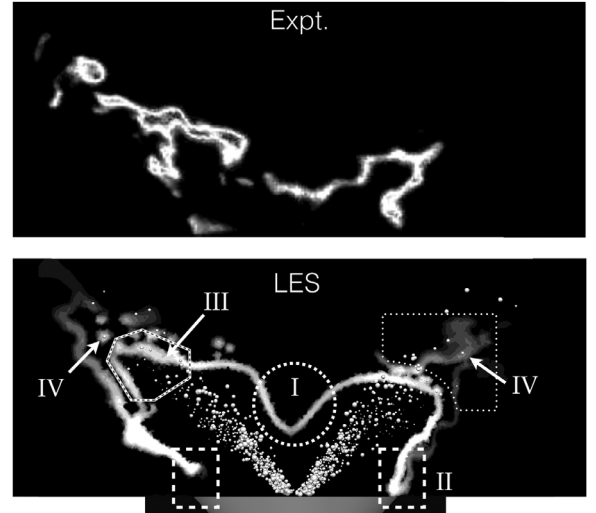


Fig. 11. Two-phase reacting case: LES-DPS versus experiment. Top : instantaneous OH-PLIF image [20]. Bottom: instantaneous field of heat-release (grey levels) with superimposed droplets (white).

them. The four flame zones are analyzed in detail later in this Section.

To confirm the non-premixed flame structure observed in the previous Section, the heat release rate (HRR) is multiplied by the Takeno index [59] to form the flame index:

$$I_{\text{flame}} = \frac{\nabla Y_F \cdot \nabla Y_{\text{Ox}}}{\|\nabla Y_F \cdot \nabla Y_{\text{Ox}}\|} \text{HRR} \quad (18)$$

In purely gaseous flames, a positive index I_{flame} indicates premixed combustion whereas a negative index indicates non-premixed combustion. An instantaneous field of the flame index is displayed in Fig. 12, showing a non-premixed flame front between the fuel vapor embedded in the flame envelope and the outer air. However a particular feature of two-phase flames appears, already observed in the DNS of [27], which is the presence of some premixing on the outer side of the flame. This is due to the evaporation of droplets that have crossed the flame (regions III and IV). Indeed, when simultaneous evaporation and combustion occur, mass transfer between phases may change the local fuel gradient. This premixed mixture does not contain enough fuel vapor to sustain a premixed *n*-heptane/air flame in cold conditions, but it contains



Fig. 12. Instantaneous Takeno index (Eq. (18)).

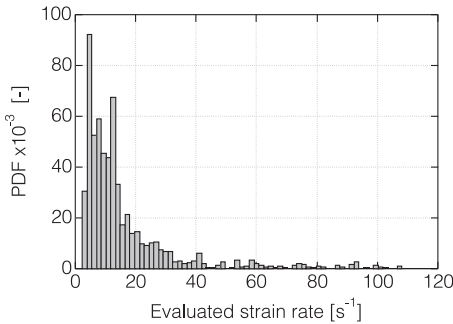


Fig. 13. Instantaneous PDF of the resolved strain rate along the stoichiometric isoline.

sufficient hot products issued from the neighboring diffusion flame to pre-heat the fuel vapor which then burns in a premixed mode. The heat release rate in this premixed zone therefore stays weak and does not significantly alter the overall non-premixed flame structure. Premixing also comes from fuel leakage at the lifted flame foot (region II). This premixing increases with the lift-off distance and participates to the flame stabilization (See Section 5.1).

The turbulent non-premixed flame may be further characterized with the strain rate along the stoichiometric line a_{st} . Figure 13 shows the probability density function (PDF) of the strain rate at stoichiometry evaluated on one instantaneous solution. Values up to $O(100 \text{ s}^{-1})$ are experienced by the non-premixed flame front, with a mean scalar dissipation of $O(10 \text{ s}^{-1})$. This range corresponds to moderate strain rates compared to the extinction limit of 600 s^{-1} for *n*-heptane/air flames [60]. For this range of strain

rate, the flame thickness, evaluated following the laminar flame theory as [61] $\sqrt{D/a_{st}}$ where D is the mean molecular diffusivity in the mixture, is found in the range 0.5–3.0 mm. Compared to the grid resolution of ≈ 0.2 mm, this confirms again *a posteriori* that the non-premixed flame is correctly discretized. The stoichiometric strain rate can also be compared to the chemical time scale to give a Damköhler number expressing the effect of the unsteady flow on the flame and the turbulent flame regime. Here the Damköhler number is in the range of few hundreds, indicating a thin wrinkled flamelet regime.

5.1. Purely gaseous flames: regions I and II

The instantaneous flame structure in regions I and II is now analyzed in mixture fraction space and compared to laminar counterflow flames obtained with the 2S_C7H16_DP scheme in similar conditions (Table 2) and at various strain rates between 10 and 150 s^{-1} , which is the highest strain rate effectively experienced by the turbulent flame (see Fig. 13). The laminar diffusion flame structure does not change much in this range and stays in the high Damköhler, thin flame regime. Scatterplots of temperature versus mixture fraction Z are shown in Fig. 14 for regions I and II, defined with dashed boxes in Fig. 11. In both cases, as already observed in Fig. 6(b), the mixture fraction never exceeds 0.35, which corresponds to the mixing in the inner zone of the flame of about 30% of fuel vapor with 70% of hot products, consistent with the temperature of 1200 K found in this region, taking into account the evaporation heat loss.

In region I, at the center of the flame, a purely non-premixed flame occurs between the above-mentioned mixture at $Z = 0.35$ on the fuel side, and recirculating gas composed of hot products and air at the global equivalence ratio $Z_{\phi g} = 0.0111$ on the oxidizer side. In the oxidizer and reacting zone, all points are concentrated along the low-strain laminar counterflow flame curve, which is consistent with the fact that this flame experiences small strain rates and weak turbulent activity. In the fuel zone, heat losses decrease the temperature below the gaseous flame curve by up to 500K. This is due to evaporation, which lowers the temperature with a maximum decrease of $\Delta T_{evap} = L_v Z / C_p = 100 \text{ K}$ at $Z = 1$. The rest of the temperature difference is explained by additional heat losses occurring along the bluff-body surface, decreasing with the distance to the bluff-body as indicated by the color scale in Fig. 14(a). The low temperature limit in the fuel side indicates the maximum fuel vapor concentration obtained for a given temperature and corresponds to the temperature-controlled evaporation limit. The stabilization of the flame in this region is ensured by the IRZ, which maintains the stoichiometric line by air and hot gas recirculation. This mechanism of stabilization by a central recircu-

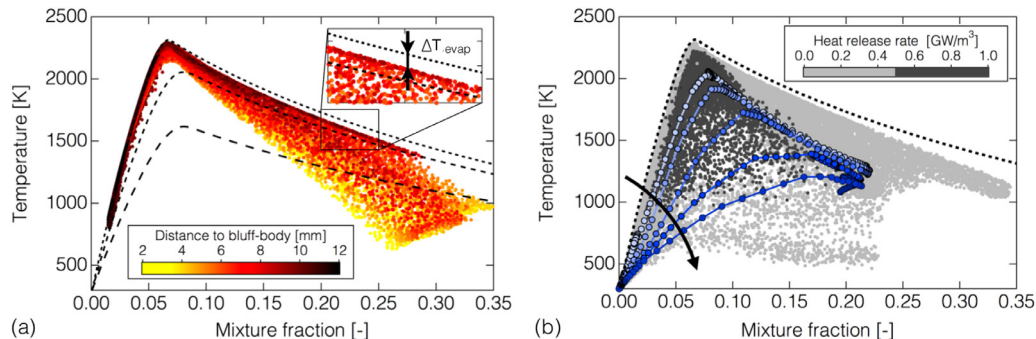


Fig. 14. Scatterplots of temperature in mixture fraction space: (a) Region I, colored by the distance from the bluff-body. Dashed lines correspond to laminar counterflow flames at increasing strain rate (10 to 150 s^{-1}); (b) Region II, with high reactivity points ($HR > 5 \times 10^8$) in black and low ones ($HR < 5 \times 10^8$) in grey. Blue lines with symbols represent the flamelets extracted from the LES-DPS in the cut and along the arrows indicated in Fig. 15(a). (For interpretation of the references to color in this figure legend, the reader is referred to the web version of this article.)

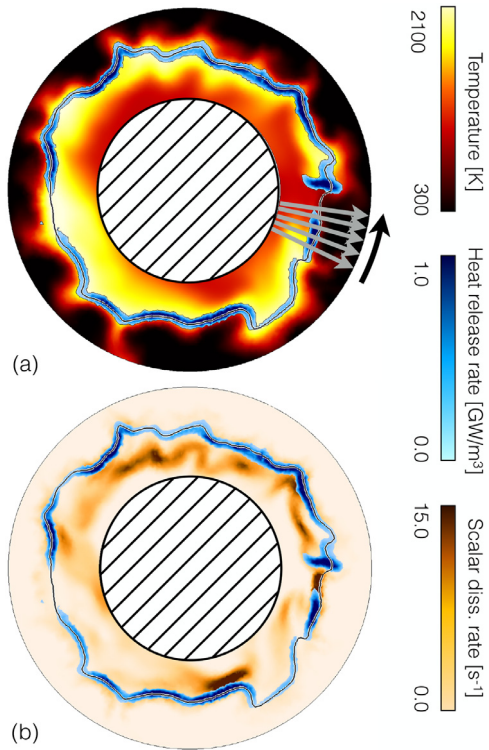


Fig. 15. Horizontal cut through Region II (4mm above the bluff body) colored by instantaneous temperature (a) and scalar dissipation rate (b). The stoichiometric line (black) and heat release rate (above $5 \times 10^7 \text{ W/m}^3$) in blue scale are also shown. (For interpretation of the references to color in this figure legend, the reader is referred to the web version of this article.)

lation zone is well-known and very similar to what is observed in swirled gaseous flames.

Region II corresponds to the sides of the conical flame and stabilizes along the outer radius of the bluff-body, between the rich inner mixture at $Z = 0.35$ and the incoming fresh air at $Z = 0$ (Fig. 11). In this region, data points are much scattered and fill the whole space. This large scatter can not be solely attributed to fluctuating strain rates, which mostly stays below 40 s^{-1} (Fig. 13), i.e., with limited impact on the flame structure. It rather indicates partial premixing, due to the intermittent flame lift-off already observed in Fig. 12. As illustrated by the blue curves of Fig. 14(b) representing quenching flamelets, this flame lift-off leads locally to cold, non-burning mixture of reactants. In the present case, flame lift-off is enhanced by heat losses at the bluff-body surface, evaluated at $\approx 0.4 \text{ MW/m}^2$, i.e., approximately 30% of the areal flame power, estimated at 1.25 MW/m^2 (based on the total flame power of 5.4 kW for a total flame surface area of $4 \times 10^{-3} \text{ m}^2$). Note however that the axisymmetric M-flame never detaches completely, although the lift-off height might be locally high, as there are always parts of the edge flame that are anchored to the wall. It is also interesting to notice that, contrary to region I, no cooling by evaporation is visible in region II: indeed, as shown in Fig. 11, region II lies outside the spray and does not experience evaporation.

Figure 15 shows instantaneous fields of temperature and scalar dissipation rate in a horizontal cut at 4 mm above the bluff body, with the stoichiometric line (black) and heat release rate (above $5 \times 10^7 \text{ W/m}^3$) in blue scale. The reaction zone appears strongly correlated with the scalar dissipation rate, with thinner, more reactive flames at high dissipation rates as expected from theory. This correlation is quantitatively revealed by the scatter plot of temperature colored with scalar dissipation rate in Fig. 16. At the particular instant shown in Fig. 15, the flame front is broken at two

locations. On the right side, the detached flame allows mixing between cold unburnt gases and hot burnt gases. At the flame edges, triple flames form (only one is visible on the Figure) and propagate along the stoichiometric line. On the left side, the flame is not quenched as indicated by the high temperature, but the low scalar dissipation rate induces a heat release rate below the threshold value used for visualization.

5.2. Two-phase combustion regimes: regions III and IV

Both regions III and IV lie inside the spray and the simultaneous droplet evaporation and combustion generate a complex flame structure. Region III contains the flame front, while region IV only sees post-combustion. In practice, it is difficult to distinguish between these two regions because of the flame large azimuthal asymmetry induced by the intermittent vortex detachment described in Fig. 7. The scatter plot of Fig. 16(a) for both regions III and IV is found relatively similar to region II. Points around and above stoichiometry correspond to region III while points below stoichiometry correspond to region IV. Due to the presence of the spray, higher mixture fractions up to 0.38 are observed compared to region II. The flame clearly has a non-premixed behavior, close to laminar strained diffusion flames, with some dispersion on the far rich side due to evaporation cooling. Some premixing also appears, resulting from the local quenching induced by the intermittent vortex detachment (Fig. 7).

The presence of droplets inside the reaction zone, where they continue to evaporate, has two effects. First, part of the released fuel vapor is instantaneously burnt, increasing significantly the heat release rate without increasing the fuel vapor concentration, and therefore the scalar dissipation rate. In other words, the heat release rate is higher, at a given mixture fraction, than in the gaseous flame at the same mixture fraction and dissipation rate. To quantify this effect, a modified mixture fraction Z' is introduced to take into account the evaporated fuel vapor that is burnt instantaneously and is not included in Z . Assuming a small fuel vapor quantity to add, this is achieved by modifying all mass fractions as:

$$Y_k' = Y_k \left(1 - \min \left(Y_{Fvap}, Y_{Fvap} \frac{\tau_v}{\tau_c} \right) \right) + \delta_{k,F} \min \left(Y_{Fvap}, Y_{Fvap} \frac{\tau_v}{\tau_c} \right) \quad (19)$$

where Y_{Fvap} is the liquid content in vapor phase, $\tau_v = \rho / S_{Fuel}^{l \rightarrow g}$ is the evaporation characteristic time (Eq. (17)), and the characteristic combustion time $\tau_c = 3.0 \times 10^{-6} \text{ s}$ is estimated from batch reactor simulations. In Eq. (19), the quantity $Y_{Fvap} \tau_v / \tau_c$ corresponds to the fuel vapor that burns instantaneously. If $\tau_v \ll \tau_c$, the quantity Y_{Fvap} is fully transferred to the gas and appears in Z , which then gives the correct fuel content. Therefore there is no evaporation effect to take into account, as reflected by Eq. (19) with $\tau_v / \tau_c \rightarrow 0$. On the contrary, when $\tau_v > \tau_c$, all the evaporated fuel is consumed as soon as produced and does not impact Z despite the fuel vapor increase. In Eq. (19) this corresponds to $\tau_v / \tau_c \rightarrow \infty$, i.e., the quantity Y_{Fvap} fully burnt instantaneously and added to the mixture fraction Z' . The impact of this mixture composition modification is shown in Fig. 17 with the heat release rate at stoichiometry plotted versus the scalar dissipation rate and colored by \tilde{Z}' / \tilde{Z} for region III. The deviation from the gaseous flame appears clearly to increase with the ratio \tilde{Z}' / \tilde{Z} , leading to higher heat release rate at given Z for the two-phase flame.

The second effect of a liquid fuel, already observed in previous experiments [62], is the local increase of equivalence ratio around the droplets, which modifies the stoichiometric line and may increase the flame front wrinkling. In the present case, this effect is moderate in region III, as can be seen for example in Fig. 11. The reason is that the spray is still dense in this region, leading to quite homogeneous evaporation in average. Inhomogeneity linked

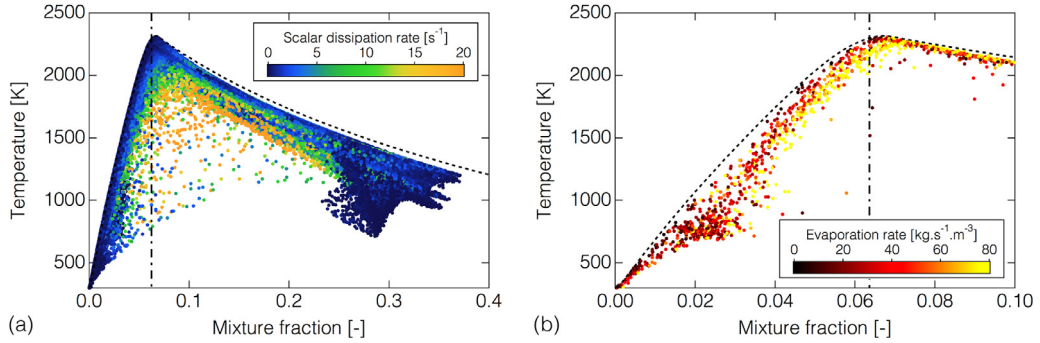


Fig. 16. Scatterplots of temperature in mixture fraction space: (a) Regions III and IV, colored by the scalar dissipation rate; (b) Zoom on Region IV, with only non-zero evaporation points. The dashed line corresponds to the laminar counterflow flame at low strain rate. (For interpretation of the references to color in this figure legend, the reader is referred to the web version of this article.)

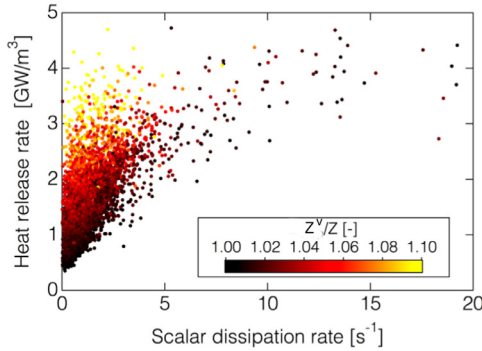


Fig. 17. Heat release rate at stoichiometry as a function of the scalar dissipation rate, colored by the ratio \tilde{Z}'/\tilde{Z} in region III. (For interpretation of the references to color in this figure legend, the reader is referred to the web version of this article.)

to individual droplets appears more clearly in region IV, and is described below.

Region IV lies outside the M-flame in the wake of region III. It is characterized by the presence of few droplets that have survived the flame and arrive in the oxidizer side, where cold air mixes with hot products. In this environment the droplets continue to evaporate and feed a very small, local flame where the temperature remains sufficiently high. Figure 16(b) shows a zoom of the scatterplot of Fig. 16(a) on the lean side corresponding to region IV, with only non-zero evaporation points. On the very lean side, evaporating fuel is found to burn in a lean premixed regime. This combustion regime is further detailed in Fig. 18 showing the temperature, species mass fractions, mixture fraction, evaporation and heat release rate profiles along a line crossing the main diffusion flame front and an isolated burning droplet burning in region IV. The heat release rate and evaporation rate profiles clearly show two distinct peaks of similar amplitude. The first peak of heat release rate is located at stoichiometry (highlighted in pink) and corresponds indeed to the main diffusion flame front. The second peak coincides with the second peak of evaporation (highlighted in blue), in a zone where the reactants are mixed. At this location, the individual droplet evaporates and the fuel vapor mixes with the local air and burns. Note the very low fuel mass fraction at this location, resulting from the instantaneous combustion of the evaporated fuel.

This local feature can be observed on the instantaneous OH-PLIF image (Fig. 11), showing very small burning pockets in region IV. However individual droplet burning only occurs in a non-premixed flame surrounding the droplet. In the present simulation, the premixed burning mode is the result of the point source approximation, with no direct representation of the droplet surface. As a consequence the evaporated fuel mixes instantaneously with the local gas instead of diffusing from the droplet surface, and then burns

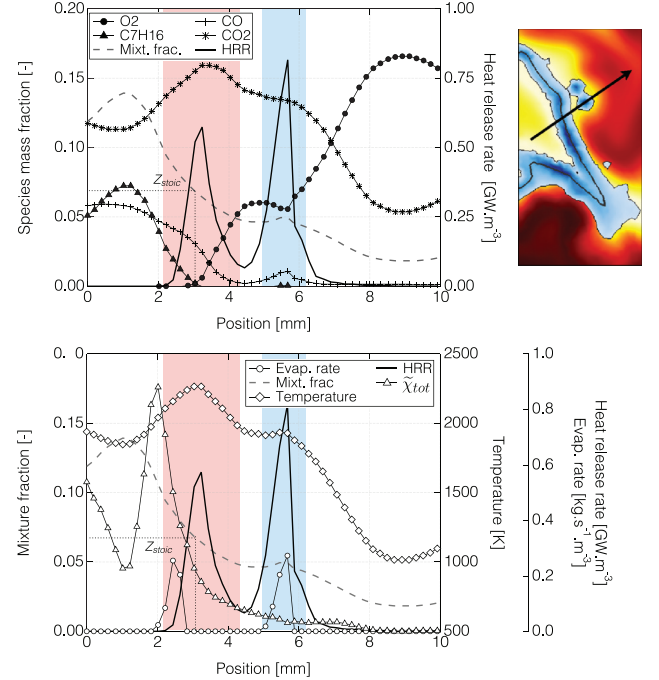


Fig. 18. Profiles of temperature, species mass fractions, mixture fraction, evaporation and heat release rate in region IV, along the line shown in the top right figure.

in a premixed mode instead of non-premixed. This may result in significant deviation of the burning rate and is analyzed in more detail in the next Section. Note also that individual droplet burning with the point source approximation may lead to numerical difficulties associated to localized strong source terms, which increase when refining the mesh unless an additional diffusion process is applied.

5.2.1. Analysis of two-phase combustion regimes

As seen in the previous sections, two-phase combustion may occur in various regimes, from fully pre-evaporated combustion to individual droplet burning, with intermediate regimes where droplets interact with the flame front. These regimes may be characterized with the group number G , first defined by Chiu and Liu [63] and later extended in [3,27,64], which compares the ratio of the droplet evaporation rate to the diffusive transport of gaseous species. It was expressed in [63] as:

$$G = 3 \left(1 + 0.276 Re_p^{1/2} Sc_F^{1/3} \right) Le_F \frac{N}{D} d_p \quad (20)$$

where N is the number of droplets in a droplet cloud of diameter D , Re_p is the droplet Reynolds number, Sc_F is the fuel Schmidt

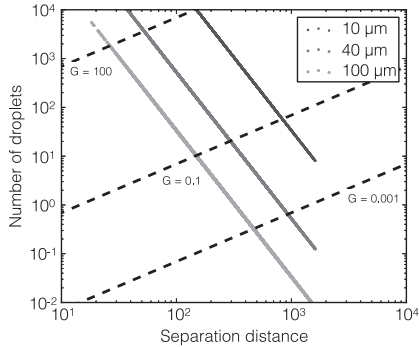


Fig. 19. Combustion diagram of the present configuration according to the group number, for three different diameters.

number and Le_F is the Lewis fuel number. In the present case, D is chosen as the average width of the hollow cone spray, which is approximately 1 cm. The non-dimensional separation distance $S = D/N^{1/3}d_p$, may be introduced to write:

$$G = 3 \left(1 + 0.276 Re_p^{1/2} Sc_F^{1/3} \right) Le_F \frac{N^{2/3}}{S} \quad (21)$$

It was demonstrated in [63,65] that single droplet combustion occurs for $G \leq 10^{-2}$. When G increases, the regime changes to group internal combustion, where burning droplets interact, until G reaches 0.1. External group combustion with evaporating droplets and a flame outside the cloud then occurs up to $G = 100$. Finally above 100, the regime corresponds to external sheath combustion with both evaporation and combustion occurring outside the cloud. In a $\log(N) - \log(S)$ diagram, constant G delineates the various regimes with lines of slope $3/2$, while constant d_p leads to lines of slope -3 . Figure 19 reports such lines for the present configuration, with 3 values of G delimiting the three regimes described above, and for small, medium and large droplet diameters as found in the configuration, i.e., 10, 40 and 100 μm . It is found that all two-phase combustion regimes may occur for the largest droplets, while the smallest ones can not burn individually. Note however that this analysis does not take into account the local gaseous conditions surrounding the spray.

From single droplet combustion analysis [66], the flame diameter d_f of the spherical flame stabilizing around the droplet can be evaluated as:

$$d_f = d_p \left[1 - \frac{\ln(1 - Y_F^{\text{surf}})}{\ln(1 + Y_0^{\infty}/s)} \right] \quad (22)$$

where Y_F^{surf} is the fuel mass fraction at the droplet surface at saturation and liquid wet-bulb temperature, Y_0^{∞} is the surrounding

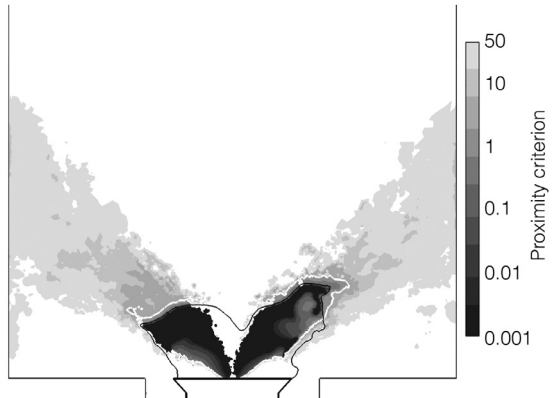


Fig. 20. Instantaneous field of the proximity criterion Sdp/d_f . The white line corresponds to $Sdp/d_f = 1$. Stoichiometry is indicated with the black line.

oxidizer mass fraction and s is the mass stoichiometric ratio. Following spray percolation theories [7,67], if $Sdp/d_f \gtrsim 1$, single droplet combustion may occur. Otherwise, the droplet can no longer be considered isolated and burns in a group combustion mode.

An instantaneous view of the proximity criterion Sdp/d_f in the configuration studied in this work is displayed Fig. 20. Inside the M-flame, the criterion is very small and single droplet combustion cannot occur. The reason is twofold: the spray is dense (small S) and no oxidizer is found (infinite d_f). The limit $Sdp/d_f = 1$ is found along a line closely following the main flame, i.e., as soon as S increases enough and air is found in sufficient amount. Outside this line, a transition region appears where the combustion regime progressively moves from group to isolated combustion, according to the inter-droplet spacing increase and the dilution with fresh air.

This analysis can be pushed further to detail the isolated combustion regime, following the work of Huang and Chiu [23], who proposed a series of correlated criteria derived from extensive DNS of isolated burning droplets. Three possible burning modes are highlighted: (i) standard pre-vaporization and premixed combustion (as modeled in the present simulation), (ii) wake flame, where a flame stands at some distance downstream in the droplet wake,

Table 3
Fitted chemistry coefficient for the reduced mechanism 2S_C7H_16_DP.

	Reaction 1	Reaction 2
Pre-exponential A_j	1.4×10^{11}	5.0×10^9
Activation temperature T_{aj}	29,000 K	21,000 K
Reaction exponents	$n_f = 0.6$	$n_{CO} = 1$
	$n_{O_2,1} = 0.9$	$n_{O_2,2} = 0.5$

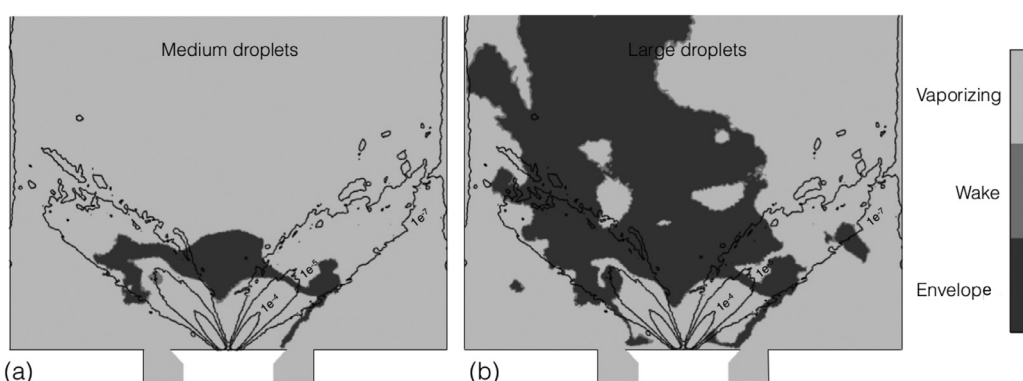


Fig. 21. Index of Group Combustion [70] for medium (40 μm) and large (100 μm) droplets. Three modes are possible : vaporizing droplet, wake flame and envelope flame. The spray position is indicated with iso-contours of liquid volume fraction.

Table 4

Coefficients of PEA function (Eqs. (25)–(27)) for 2S_C7H16_DP.

	$\Phi_{0,j}$	$\sigma_{0,j}$	B_j	$\Phi_{1,j}$	$\sigma_{1,j}$	C_j	$\Phi_{2,j}$	$\sigma_{2,j}$	$\Phi_{3,j}$	$\sigma_{3,j}$
$j = 1$	1.1635	0.0518	1.131	1.243	0.101	$1.2e^4$	1.494	0.0082	–	–
$j = 2$	1.146	0.045	$1.5e^{-4}$	1.2	0.04	0.035	1.215	0.03	1.32	0.09

and (iii) envelope flame surrounding the droplet. Criteria are based on a Damköhler number previously proposed by Law [68] and extended by Mawid and Aggarwal [69], which compares the diffusion and chemical time-scales. This approach is applied *a posteriori* on the present LES-DPS results, and is illustrated for one instantaneous solution in Fig. 21 for both medium (40 μm) and large droplets (100 μm) which have the capacity to survive in the post-flame region and undergo individual burning. Consistently with the proximity criterion, the pre-vaporizing mode dominates inside the M-flame where single droplet burning is not possible. Outside the M-flame, the envelope mode is mostly encountered in the IRZ, where local conditions allow single droplet combustion. The occurrence of envelope flames increases with the droplet size. The wake flame mode is on the contrary very rare. This is explained by the droplet slip velocity, necessary to sustain a wake, and which is small outside the M-flame where droplets have reached mechanical equilibrium.

The combined results on the proximity criterion and the analysis with criteria from Huang and Chiu [23] allow to conclude that single droplet combustion in an envelope flame mode effectively occurs in region IV. The burning rate of these droplets is therefore controlled by their evaporation and significantly differ from a premixed burning mode. This calls for a specific model for individual droplet burning, which will be developed in future work.

6. Conclusions

In this study, LES-DPS of a spray swirled burner has been performed and compared with experiment. Good quantitative agreement in terms of velocity profiles, spray shape, and flame structure has been obtained. Observed slight discrepancies may be attributed to uncertainties on liquid injection, and it would be also interesting to confirm the results with a more detailed description of combustion chemistry instead of the two-step mechanism used here. The analysis shows a complex, mainly non-premixed flame structure, yielding various combustion modes. Pre-evaporated, purely gaseous flames are shown to have strained diffusion and partially premixed behaviors. When the spray directly interacts with the flame, several different two-phase combustion regimes appear, depending on the droplet size and separation distance. One particular feature of this experiment is the occurrence of single droplet combustion. Unfortunately, the LES grid does not allow to describe the non-premixed flame that stabilizes close around the droplet. Instead the current model leads to premixed combustion, with possible significant error on the burning rate and combustor efficiency. If a sufficient amount of liquid fuel burns in individual droplets, it is necessary then to use a single droplet combustion model adapted to the LES-DPS framework. The development of such model is the topic of future work.

Declaration of Competing Interest

None.

Acknowledgments

This work was made possible thanks to the fruitful collaboration with D.E Cavalieri, A. Tyliszczak and Pr. E. Mastorakos from

the University of Cambridge and performed using HPC resources from GENCI (Grant A0032B10157).

Appendix A. Reduced chemistry details

The reaction rates of Eq. (5) are written in the classical Arrhenius form:

$$k_{f,1} = A_1 f_1(\Phi) \exp(-T_{a1}/T) [C_7H_{16}]^{n_f} [O_2]^{n_{o_2,1}}, \quad (23)$$

$$k_{f,2} = A_2 f_2(\Phi) \exp(-T_{a2}/T) [C_0]^{n_{co}} [O_2]^{n_{o_2,2}}, \quad (24)$$

The fitted chemistry coefficient are given in Table 3, using a Arrhenius law formulation.

The correction functions of the pre-exponential factor in order to recover the correct flame speed for rich mixtures (methodology from [47]) have the following form:

$$f_1(\Phi) = \frac{2}{[1 + \tanh(\frac{\Phi_{0,1} - \Phi}{\sigma_{0,1}})] + B_1[1 + \tanh(\frac{\Phi - \Phi_{1,1}}{\sigma_{1,1}})] + C_1[1 + \tanh(\frac{\Phi - \Phi_{2,1}}{\sigma_{2,1}})]} \quad (25)$$

$$f_2(\Phi) = \frac{1}{2} \left[1 + \tanh \left(\frac{\Phi_{0,2} - \Phi}{\sigma_{0,2}} \right) \right] + \frac{B_2}{2} \left[1 + \tanh \left(\frac{\Phi - \Phi_{1,1}}{\sigma_{1,1}} \right) \right] \quad (26)$$

$$+ \frac{C_2}{2} \left[1 + \tanh \left(\frac{\Phi - \Phi_{2,2}}{\sigma_{2,2}} \right) \right] \times \left[1 + \tanh \left(\frac{\Phi_{3,2} - \Phi}{\sigma_{3,2}} \right) \right] \quad (27)$$

Their parameters are summarized in Table 4:

References

- [1] P. Jenny, D. Roekaerts, N. Beishuizen, Modeling of turbulent dilute spray combustion, Prog. Energy Combust. Sci. 38 (2012) 846–887.
- [2] H.H. Chiu, Advances and challenges in droplet and spray combustion. I. Toward a unified theory of droplet aerothermochemistry, Prog. Energy Combust. Sci. 26 (2000) 381–416.
- [3] K. Annamalai, W. Ryan, Interactive processes in gasification and combustion. Part 1: liquid drop arrays and clouds, Prog. Energy Combust. Sci. 18 (1992) 221–295.
- [4] B. Vieille, C. Chauveau, X. Chesneau, A. Odeode, I. Gokalp, High-pressure droplet burning experiments in microgravity, Symp. (Int.) Combust. 26 (1996) 1259–1265.
- [5] V. Raghavan, V. Babu, T. Sundararajan, R. Natarajan, Flame shapes and burning rates of spherical fuel particles in a mixed convective environment, Int. J. Heat Mass Transf. 48 (2005) 5354–5370.
- [6] M. Mikami, H. Oyagi, N. Kojima, Y. Wakashima, M. Kikuchi, S. Yoda, Microgravity experiments on flame spread along fuel-droplet arrays at high temperatures, Combust. Flame 146 (2006) 391–406.
- [7] A. Umemura, S. Takamori, Percolation theory for flame propagation in non- or less-volatile fuel spray: a conceptual analysis to group combustion excitation mechanism, Combust. Flame 141 (2005) 336–349.
- [8] D.R. Ballal, A.H. Lefebvre, Flame propagation in heterogeneous mixtures of fuel droplets, fuel vapor and air, Symp. (Int.) Combust. 18 (1981) 321–327.
- [9] A. Neophytou, E. Mastorakos, Simulations of laminar flame propagation in droplet mists, Combust. Flame 156 (2009) 1627–1640.
- [10] S.K. Marley, E.J. Welle, K.M. Lyons, W.L. Roberts, Effects of leading edge entrainment on the double flame structure in lifted ethanol spray flames, Exp. Therm. Fluid Sci. 29 (2004a) 23–31.
- [11] S.K. Marley, K.M. Lyons, K.A. Watson, Leading-edge reaction zones in lifted-Jet gas and spray flames, Flow Turbul. Combust. 72 (2004b) 29–47.

- [12] S. Elghobashi, G.C. Truesdell, On the two-way interaction between homogeneous turbulence and dispersed solid particles. I: turbulence modification, *Phys. Fluids* 5 (1993) 1790–1801.
- [13] C. Pichard, Y. Michou, C. Chauveau, I. Gokalp, Average droplet vaporization rates in partially prevaporized turbulent spray flames, *Proc. Combust. Inst.* 29 (2002) 527–533.
- [14] J.D. Gounder, A. Kourmatzis, A.R. Masri, Turbulent piloted dilute spray flames: flow fields and droplet dynamics, *Combust. Flame* 159 (2013) 3372–3397.
- [15] A. Kourmatzis, W. O'Loughlin, A.R. Masri, Effects of turbulence, evaporation and heat release on the dispersion of droplets in dilute spray jets and flames, *Flow Turbul. Combust.* 91 (2013) 405–427.
- [16] J.F. Widmann, C. Presser, A benchmark experimental database for multiphase combustion model input and validation, *Combust. Flame* 129 (2002) 47–86.
- [17] C. Presser, A benchmark experimental database for multiphase combustion model input and validation: a users follow-up, 2005. 4th Joint Meeting of the US Sections of the Combustion Institute, The Combustion Institute, Pittsburgh.
- [18] M. Sanjosé, T. Lederlin, L. Gicquel, B. Cuenot, H. Pitsch, N. García-Rosa, R. Lecourt, T. Poinsot, LES of two-phase reacting flows, Summer Program, Center for Turbulence Research, NASA Ames/Stanford Univ. (2008), pp. 251–263.
- [19] T. Marchione, S.F. Ahmed, E. Mastorakos, Ignition of turbulent swirling n-heptane spray flames using single and multiple sparks, *Combust. Flame* 156 (2009) 166–180.
- [20] D.E. Cavalieri, J. Kariuki, E. Mastorakos, A comparison of the blow-off behaviour of swirl-stabilized premixed, non-premixed and spray flames, *Flow Turbul. Combust.* 91 (2013) 347–372.
- [21] G. Wu, W.A. Sirignano, Transient burning of a convective fuel droplet, *Combust. Flame* 157 (2010) 970–981.
- [22] G. Wu, W.A. Sirignano, Transient convective burning of interactive fuel droplets in double-layer arrays, *Combust. Flame* 158 (2011) 2395–2407.
- [23] J.S. Huang, H.H. Chiu, Multistate behavior of a droplet in dilute sprays, *Atom. Sprays* 7 (1997) 479–506.
- [24] C.H. Beck, R. Koch, H.J. Bauer, Identification of droplet burning modes in lean, partially prevaporized swirl-stabilized spray flames, *Proc. Combust. Inst.* 32 (2009) 2195–2203.
- [25] S. Sazhin, Advanced models of fuel droplet heating and evaporation, *Prog. Energy Combust. Sci.* 32 (2006) 162–214.
- [26] J. Réveillon, F.X. Demoulin, Effects of the preferential segregation of droplets on evaporation and turbulent mixing, *J. Fluid Mech.* 583 (2007) 273–302.
- [27] J. Réveillon, L. Vervisch, Analysis of weakly turbulent diluted-spray flames and spray combustion regimes, *J. Fluid Mech.* 537 (2005) 317–347.
- [28] P. Domingo, L. Vervisch, J. Réveillon, DNS analysis of partially premixed combustion in spray and gaseous turbulent flame-bases stabilized in hot air, *Combust. Flame* 140 (2005) 172–195.
- [29] Y. Baba, R. Kurose, Analysis and flamelet modelling for spray combustion, *J. Fluid Mech.* 612 (2008) 45–79.
- [30] A. Fujita, H. Watanabe, R. Kurose, S. Komori, Two-dimensional direct numerical simulation of spray flames – part 1: effects of equivalence ratio, fuel droplet size and radiation, and validity of flamelet model, *Fuel* 104 (2013) 515–525.
- [31] T. Kitano, T. Nakatani, R. Kurose, S. Komori, Two-dimensional direct numerical simulation of spray flames – part 2: effects of ambient pressure and lift, and validity of flamelet model, *Fuel* 104 (2013) 526–535.
- [32] G. Borghesi, E. Mastorakos, R.S. Cant, Complex chemistry DNS of n-heptane spray autoignition at high pressure and intermediate temperature conditions, *Combust. Flame* 160 (2013) 1254–1275.
- [33] K. Luo, O. Desjardins, H. Pitsch, DNS of droplet evaporation and combustion in a swirling combustor, Annual Research Briefs, Center for Turbulence Research, Stanford Univ., 2008, pp. 235–265.
- [34] A. Sadiki, W. Ahmadi, M. Chrigui, J. Janicka, Toward the impact of fuel evaporation-combustion interaction on spray combustion in gas turbine combustion chambers. part i: Effect of partial fuel vaporization on spray combustion, Experiments and Numerical Simulations of Diluted Spray Turbulent Combustion, Springer (2011), pp. 69–110.
- [35] K. Li, L.X. Zhou, C.K. Chan, Large-eddy simulation of ethanol spray combustion using a finite-rate combustion model, International Symposium on Coal Combustion, Springer (2013), pp. 105–109.
- [36] W.P. Jones, A.J. Marquis, K. Vogiatzaki, Large-eddy simulation of spray combustion in a gas turbine combustor, *Combust. Flame* 161 (2014) 222–239.
- [37] A. Giusti, E. Mastorakos, Detailed chemistry LES/CMC simulation of a swirling ethanol spray flame approaching blow-off, *Proc. Combust. Inst.* 36 (2) (2017) 2625–2632.
- [38] F. Shum-Kivan, J.M. Santiago, A. Verdier, E. Riber, B. Renou, G. Cabot, B. Cuenot, Experimental and numerical analysis of a turbulent spray flame structure, *Proc. Combust. Inst.* 36 (2) (2017) 2567–2575.
- [39] L. Ma, D. Roekaerts, Numerical study of the multi-flame structure in spray combustion, *Proc. Combust. Inst.* 36 (2) (2017) 2603–2613.
- [40] D. Tylliszczak, A. Cavalieri, E. Mastorakos, LES/CMC of blow-off in a liquid fueled swirl burner, *Flow Turbul. Combust.* 92 (1–2) (2014) 237–267.
- [41] D. Cavalieri, Blow-off in gas turbine combustors, University of Cambridge, 2013 Ph.d. thesis.
- [42] W. Sutherland, The viscosity of gases and molecular force, *Philos. Mag.* 5 (1893) 507–531.
- [43] F. Nicoud, F. Ducros, Subgrid-scale stress modelling based on the square of the velocity gradient tensor, *Flow Turbul. Combust.* 62 (1999) 183–200.
- [44] A. code, http://www.cerfacs.fr/cfd/avbp_code.php and <http://www.cerfacs.fr/cfd/cfdpublications.html>.
- [45] O. Colin, M. Rudgyard, Development of high-order Taylor-Galerkin schemes for LES, *J. Comput. Phys.* 162 (2000) 338–371.
- [46] B. Franzelli, E. Riber, M. Sanjosé, T. Poinsot, A two-step chemical scheme for large-eddy simulation of kerosene-air flames, *Combust. Flame* 157 (2010) 1364–1373.
- [47] E. Fernández-Tarrazo, A.L. Sánchez, A. Liñán, F.A. Williams, A simple one-step chemistry model for partially premixed hydrocarbon combustion, *Combust. Flame* 147 (2006) 32–38.
- [48] D. G. Goodwin, Cantera c++ users guide, 2002, <http://sourceforge.net/projects/canterra>.
- [49] A.J. Smallbone, W. Liu, C.K. Law, X.Q. You, H. Wang, Experimental and modeling study of laminar flame speed and non-premixed counterflow ignition of n-heptane, *Proc. Combust. Inst.* 32 (2009) 1245–1252.
- [50] L. Schiller, A. Nauman, A drag coefficient correlation, *VDI Zeitung* 77 (1935) 318–320.
- [51] B. Abramzon, W.A. Sirignano, Droplet vaporisation model for spray combustion calculations, *Int. J. Heat Mass Transf.* 9 (1989) 1605–1618.
- [52] P.S. Sánchez, Modeling the dispersion and evaporation of sprays in aeronautical combustion chambers, INPT, 2012.
- [53] G. Hannebique, P. Sierra, E. Riber, B. Cuenot, Large eddy simulation of reactive two-phase flow in a aeronautical multipoint burner, *Flow Turbul. Combust.* 90 (2012) 449–469.
- [54] R. Garagnol, The faxén formulae for a rigid particle in an unsteady non-uniform Stokes flow, *J. Méc. Théor. Appl.* 1 (2) (1983) 143–160.
- [55] M. Maxey, J. Riley, Equation of motion for a small rigid sphere in a nonuniform flow, *Phys. Fluids* 26 (1983) 883–889.
- [56] F. Jaegle, J.-M. Senoner, M. Garcia, F. Bismes, R. Lecourt, B. Cuenot, T. Poinsot, Lagrangian and Eulerian simulations of evaporating fuel spray in an aeronautical multipoint injector, *Proc. Combust. Inst.* 33 (2011) 2099–2107.
- [57] T. Poinsot, S. Lele, Boundary conditions for direct simulations of compressible viscous flows, *J. Comput. Phys.* 101 (1992) 104–129.
- [58] R.W. Bilger, A mixture fraction framework for the theory and modeling of droplets and sprays, *Combust. Flame* 158 (2011) 191–202.
- [59] T. Takeno, M. Murayama, Y. Tanida, Fractal analysis of turbulent premixed flame surface, *Exp. Fluids* 10 (1990) 61–70.
- [60] R. Seiser, H. Pitsch, K. Seshadri, W.J. Pitz, H.J. Gurran, Extinction and autoignition of n-heptane in counterflow configuration, *Proc. Combust. Inst.* 28 (2) (2000) 2029–2037.
- [61] T. Poinsot, D. Veynante, Theoretical and numerical combustion, 2011. Third Edition (<http://www.cerfacs.fr/elearning>)
- [62] X. Mercier, M. Orain, F. Grisch, Investigation of droplet combustion in strained counterflow diffusion flames using planar laser-induced fluorescence, *J. Phys. A: Chem.* 88 (2007) 151–160.
- [63] H. Chiu, T. Liu, Group combustion of liquid droplets, *Combust. Sci. Tech.* 17 (1977) 127–131.
- [64] J. Urzay, A revised spray-combustion diagram of diffusion-controlled burning regimes in fuel-spray clouds, Annual Research Brief, Center for Turbulence Research, 2011, pp. 193–198.
- [65] H.H. Chiu, H.Y. Kim, E.J. Croke, Internal group combustion of liquid droplets, *Symp.(Int.) Combust.* 19 (1982) 971–980.
- [66] W.A. Sirignano, Fluid dynamics and transport of droplets and sprays, Cambridge University Press, 1999.
- [67] A.R. Kerstein, C.K. Law, Percolation in combusting sprays I: transition from cluster combustion to percolate combustion in non-premixed sprays, *Symp. (Int.) Combust.* 19 (1982) 961–969.
- [68] C.K. Law, Asymptotic theory for ignition and extinction in droplet burning, *Combust. Flame* 24 (1975) 89–98.
- [69] M. Mawid, S.K. Aggarwal, Analysis of dropwise ignition versus external ignition for dilute multicomponent fuel sprays, *Combust. Flame* 81 (1990) 59–72.
- [70] J.S. Huang, H.H. Chiu, Comparison of droplet combustion models in non-premixed spray combustion, 38th AIAA/ASME/SAE/ASEE Joint Propulsion Conference & Exhibit, AIAA, 2002.